

On the structural integrity and electrochemical activity of a $0.5\text{Li}_2\text{MnO}_3 \cdot 0.5\text{LiCoO}_2$ cathode material for lithium-ion batteries†

Cite this: *J. Mater. Chem. A*, 2014, 2, 9099

Jatinkumar Rana,^{*a} Richard Kloepsch,^{*b} Jie Li,^b Tobias Scherb,^a Gerhard Schumacher,^a Martin Winter^b and John Banhart^{ac}

Structural changes in a $0.5\text{Li}_2\text{MnO}_3 \cdot 0.5\text{LiCoO}_2$ cathode material were investigated by X-ray absorption spectroscopy. It is observed that both Li_2MnO_3 and LiCoO_2 components of the material exist as separate domains, however, with some exchange of transition metal (TM) ions in their slab layers. A large irreversible capacity observed during activation of the material in the 1st cycle can be attributed to an irreversible oxygen release from Li_2MnO_3 domains during lithium extraction. The average valence state of manganese ions remains unchanged at 4+ during charge and discharge. In the absence of conventional redox processes, lithium extraction/reinsertion from/into Li_2MnO_3 domains occurs with the participation of oxygen anions in redox reactions and most likely involves the ion-exchange process. In contrast, lithium deintercalation/intercalation from/into LiCoO_2 domains occurs topotactically, involving a conventional $\text{Co}^{3+}/\text{Co}^{4+}$ redox reaction. The presence of Li_2MnO_3 domains and their unusual participation in electrochemical processes enable LiCoO_2 domains of the material to sustain a higher cut-off voltage without undergoing irreversible structural changes.

Received 7th March 2014
Accepted 4th April 2014

DOI: 10.1039/c4ta01161a

www.rsc.org/MaterialsA

1 Introduction

Lithium-rich transition metal oxides with a general chemical formula $\text{Li}[\text{Li}_{1-x}\text{M}_x]\text{O}_2$ (M = TM ions) are drawing worldwide attention as candidate cathode materials for next generation lithium-ion batteries.^{1–9} They deliver reversible capacities of $\sim 250 \text{ mA h g}^{-1}$ when charged above 4.5 V, which is significantly higher than that delivered by the commercially available LiCoO_2 cathode material ($\sim 140 \text{ mA h g}^{-1}$), and exhibit high rate capabilities.⁷ Besides, these cathode materials are rich in manganese which make them cost-effective and eco-friendly.

The composition $\text{Li}[\text{Li}_{1-x}\text{M}_x]\text{O}_2$ can be written in a two-component notation as $(x)\text{Li}_2\text{MnO}_3 \cdot (1-x)\text{LiMO}_2$, where both the components can be described by a layered O3 structure. This similarity is believed to be the reason for the structural integration between the two components, but how they actually coexist in a system remains a debatable subject. Some research groups believe that these two components exist as separate domains,^{1,3,5,6,9,10} while others assume that they form a solid

solution.¹¹ Moreover, the reasons for a large irreversible capacity delivered by these materials during activation and reversible capacities of $\sim 250 \text{ mA h g}^{-1}$ during subsequent cycles remain elusive. Over the past few years, numerous contradicting mechanisms have been proposed to explain the electrochemical processes in these materials. Armstrong *et al.*¹² and Yabuuchi *et al.*¹³ proposed that an irreversible oxygen release along with lithium extraction accounts for the large irreversible capacity observed during activation of these materials. However, Hong *et al.*¹⁴ reported that it is not oxygen removal, but the metal-ligand orbital hybridization which can contribute electrons during lithium extraction without oxidizing manganese ions beyond 4+. Quite contrarily, Ohzuku *et al.*¹⁵ proposed the oxidation of octahedrally coordinated Mn^{4+} ions as one of the reasons for the large capacity delivered by these cathode materials, although such oxidation can be realized at practically unattainable potentials.¹⁶ Thus, there remains a fair amount of ambiguity towards understanding this novel class of cathode materials, both structurally and electrochemically.

In the present work, we investigate structural modifications in electrochemically cycled samples of $0.5\text{Li}_2\text{MnO}_3 \cdot 0.5\text{LiCoO}_2$ by X-ray absorption spectroscopy (XAS). The aim of the present work is to exploit the element selectivity of XAS for elucidating the structural integration between the two components of the material on an atomistic-scale and the mechanism of electrochemical activation. Changes in the average valence state, electronic configuration and local coordination symmetry of TM ions in the material during charge and discharge are

^aHelmholtz-Zentrum Berlin für Materialien und Energie, Hahn-Meitner-Platz 1, 14109 Berlin, Germany. E-mail: jatinkumar.rana@helmholtz-berlin.de

^bInstitute of Physical Chemistry, MEET Battery Research Centre, University of Muenster, Corrensstrasse 46, 48149 Muenster, Germany. E-mail: r.kloepsch@uni-muenster.de

^cTechnische Universität Berlin, Hardenbergstrasse 36, 10623 Berlin, Germany

† Electronic supplementary information (ESI) available. See DOI: 10.1039/c4ta01161a

deduced from the near-edge region of the absorption spectra, called the X-ray absorption near-edge structure (XANES). In addition, structural changes such as the number of nearest neighbors, interatomic distances and structural disorder are quantified by fitting a theoretical model to the extended region of the absorption spectra, called the extended X-ray absorption fine structure (EXAFS).

2 Experimental

The material was synthesized *via* a co-precipitation route previously reported.⁷ The mixed manganese–cobalt hydroxide precursor was precipitated from an aqueous solution of transition metal acetates ($\text{Mn}(\text{CH}_3\text{COO})_2 \cdot 4\text{H}_2\text{O}$ and $\text{Co}(\text{CH}_3\text{COO})_2 \cdot 4\text{H}_2\text{O}$; Alfa Aesar (>98%)) with a stoichiometric ratio of Mn : Co as 1 : 1 and lithium hydroxide hydrate ($\text{LiOH} \cdot \text{H}_2\text{O}$; ABCR (>98%)) under vigorous stirring. After thoroughly rinsing with distilled water, the precipitate was dried at 393 K in a vacuum overnight. The dried precipitate was then ball-milled with a stoichiometric amount of $\text{LiOH} \cdot \text{H}_2\text{O}$ for 3 h using zirconia jars and ethanol as a lubricant. After drying at room temperature, the mixture was annealed in air at 753 K for 5 h in a muffle oven. The annealed material was then pressed into pellets and calcined at 1173 K in a tube furnace for 6 h, followed by quenching in liquid nitrogen to obtain the final material. The chemical composition of the as-synthesized material was determined by inductively coupled plasma/optical emission spectrometry (ICP/OES) (SPECTRO ARCOS, Ametek, Germany), while its crystal structure was determined by powder X-ray diffraction (XRD) using a Bruker D8 Advance diffractometer equipped with a Cu K_α radiation source and a one-dimensional position sensitive detector.

Cathodes for electrochemical characterization were prepared by mixing 85 wt% active material, 5 wt% carbon black (Super C65, Timcal) and 10 wt% of a solution of polyvinylidene difluoride (Kynar® FLEX 2801, Arkema) in *N*-methyl-2-pyrrolidone (Acros Organics) acting as a binder. The resultant slurry was tape-cast on an aluminum current collector. A circular disc of 12 mm diameter was punched out of the slurry-coated aluminium current collector and constitutes the cathode in the cell. Electrochemical measurements were carried out in three-electrode Swagelok cells using metallic lithium as the counter and reference electrode. A mixture of ethylene carbonate (EC) and dimethyl carbonate (DMC) (1 : 1 V/V) containing 1 M LiPF_6 (LP30, Merck) was used as the electrolyte and a glass fiber filter (Whatman GF/D) as a separator. The cells were cycled between 2.5 V and 4.8 V *vs.* Li/Li^+ with a constant current density of 20 mA g^{-1} (*i.e.* C/10 with 1 C = 200 mA g^{-1}) using a Maccor Series 4000 battery testing unit. The cells were opened in a dry room and cathodes were washed with DMC. Once dried, the cathodes were sealed between adhesive-coated Kapton tapes to prevent exposure to air. The samples were then vacuum-sealed in a container and transported to the experimental station.

XAS measurements were carried out in the transmission mode at the Mn and Co K-edges of $0.5\text{Li}_2\text{MnO}_3 \cdot 0.5\text{LiCoO}_2$ in the pristine, charged (4.8 V) and discharged (2.5 V) states. The samples were measured at beamline KMC-2 of the BESSY-II

synchrotron light source, Berlin, Germany. The beamline is equipped with a graded Si–Ge (111) double crystal monochromator. Higher harmonics were rejected by detuning the monochromator such that the intensity of the beam on the sample was 65% of the maximum possible intensity. Absolute energy calibration of the monochromator was carried out by measuring reference foils of pure Mn and Co simultaneously with the sample. The intensities of the incident beam and beams transmitted through the sample and the reference foil were measured using gas-filled ionization chambers. In addition to the pristine, charged and discharged samples of $0.5\text{Li}_2\text{MnO}_3 \cdot 0.5\text{LiCoO}_2$, various reference compounds of Mn and Co such as Mn_2O_3 , MnO_2 -pyrolusite, Li_2MnO_3 , CoO and LiCoO_2 were also measured. All spectra were energy-calibrated with respect to the first peak in the derivative spectrum of pure elements. Various data pre-processing operations were carried out as prescribed elsewhere¹⁷ using the software ATHENA of the package IFEFFIT.¹⁸ The normalized component of the EXAFS signal was transformed to *k* space (*i.e.* wavenumber) and the resultant $\chi(k)$ signal was multiplied by k^3 to emphasize the data at high *k*. The k^3 -weighted $\chi(k)$ signal was then Fourier transformed and left uncorrected for a phase shift. A model function was generated by performing *ab initio* calculations using the code FEFF8.2 (ref. 19) and least-square fitted to the data using the software ARTEMIS of the package IFEFFIT.¹⁸ The fitting parameters involved a single amplitude reduction factor S_0^2 and an overall energy parameter ΔE_0 for each dataset. A fractional change in the bond length α_{fit} was refined for each coordination shell so that a change in the bond length ΔR was given by $\Delta R = \alpha_{\text{fit}} \times R_{\text{theory}}$. Furthermore, each coordination shell was assigned a separate mean-squared relative displacement parameter σ^2 depending on the type of the backscattering atoms it contained and its mean distance from the central absorber. The parameters for the multiple scattering paths were constrained in terms of those of the corresponding single scattering paths.²⁰ The statistical quality of an EXAFS fit was evaluated based on its *R*-factor.

3 Results

Fig. 1 demonstrates the powder XRD patterns of various lithium-rich materials along with that of the LiCoO_2 reference compound. All major reflections in the XRD patterns of lithium-rich materials can be indexed with a trigonal crystal system (space group $R\bar{3}m$). However, superlattice reflections in the 2θ range between 20° and 30° , representing the ordering of lithium and TM ions in the slab layers, can be specifically assigned to the space group $C2/m$. With increasing Co-content, all peaks in the XRD patterns of lithium-rich materials shift to a higher angle towards those of the LiCoO_2 reference compound and the superlattice reflections gradually disappear.

Fig. 2 shows the voltage *vs.* capacity profile of $0.5\text{Li}_2\text{MnO}_3 \cdot 0.5\text{LiCoO}_2$ during the 1st cycle. The cell delivered a specific capacity of 308 mA h g^{-1} when charged to 4.8 V and of 252 mA h g^{-1} when discharged to 2.5 V, with a 1st cycle efficiency of $\sim 82\%$. A large irreversible capacity thus obtained

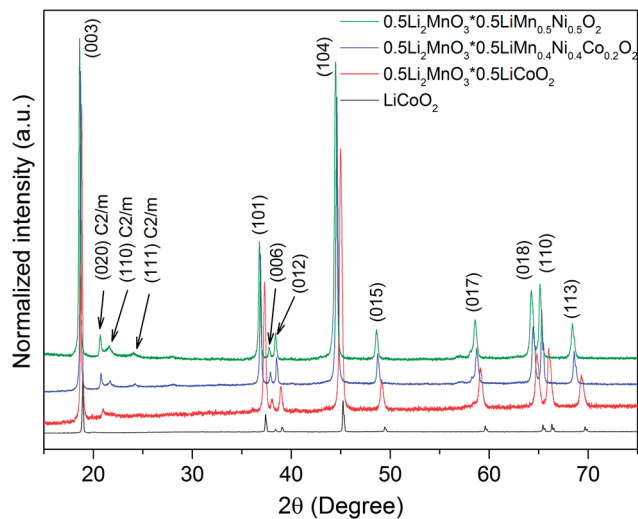


Fig. 1 Powder XRD patterns of $0.5\text{Li}_2\text{MnO}_3 \cdot 0.5\text{LiMn}_{0.5}\text{Ni}_{0.5}\text{O}_2$ (green line), $0.5\text{Li}_2\text{MnO}_3 \cdot 0.5\text{LiMn}_{0.4}\text{Ni}_{0.4}\text{Co}_{0.2}\text{O}_2$ (blue line) and $0.5\text{Li}_2\text{MnO}_3 \cdot 0.5\text{LiCoO}_2$ (red line) cathode materials along with that of the LiCoO_2 (black line) reference compound.

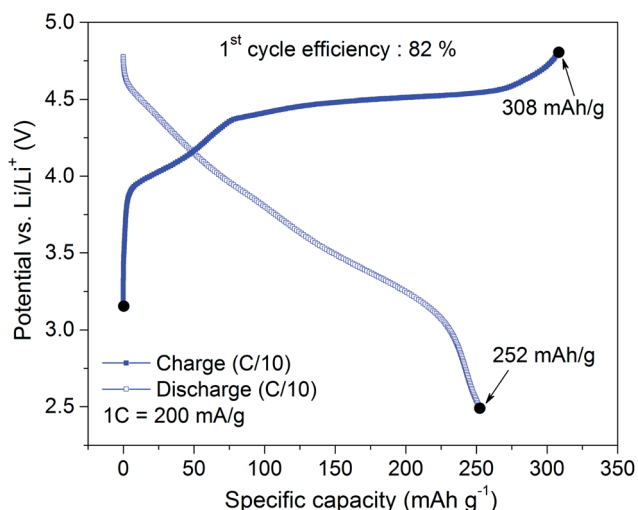


Fig. 2 Voltage vs. capacity profile of $0.5\text{Li}_2\text{MnO}_3 \cdot 0.5\text{LiCoO}_2$ during the 1st cycle. The solid circles (●) represent the states where XAS data were recorded at the Mn and Co K-edges of the material.

during activation of the material has also been reported for other lithium-rich cathode materials in the literature.^{1,3–8,10}

3.1 XANES

The normalized absorption spectra at the Mn and Co K-edges of the material are presented in Fig. 3 along with those of various reference compounds of Mn and Co. As shown in Fig. 3a, the absorption K-edge is characterized by a variety of edge-features such as an absorption threshold, a pre-edge peak corresponding to the $1s \rightarrow 3d$ transition and a vertically rising main edge with a maximum corresponding to the $1s \rightarrow 4p$ transition. A relative shift in the position of these features, called the chemical shift, provides an empirical mean of estimating changes in the

average valence state of absorbing atoms. Since outer p-orbitals are less tightly bound and, therefore, more sensitive to chemical changes than inner d-orbitals, chemical shifts observed in the position of the $1s \rightarrow 4p$ peak are relatively large. As can be seen from Fig. 3a, the position of the $1s \rightarrow 4p$ peak at the Mn K-edge of the pristine sample coincides with that of the Mn^{4+} -containing reference compound. For the charged sample, this peak shifts to higher energy and reverses to lower energy for the discharged sample. However, a consistent chemical shift is not observed at other edge-features, especially along the vertically rising main edge where spectra cross and no clear trend is observed. On the other hand, chemical shifts at the Co K-edge appear less complex; see Fig. 3b. In the pristine state, the position of the $1s \rightarrow 4p$ peak at the Co K-edge coincides with that of the LiCoO_2 reference compound. It shifts to higher energy for the charged sample and reverses to lower energy for the discharged sample. The pre-edge region at the Mn K-edge is characterized by a splitting of the $1s \rightarrow 3d$ peak into t_{2g} and e_g peaks (inset in Fig. 3a). For the charged sample, the pre-edge region is more intense and the peak splitting is less resolved. However, for the discharged sample, the intensity of the pre-edge region decreases and the peak splitting becomes clearer. On the other hand, the pre-edge region at the Co K-edge is characterized by a single peak corresponding to the $1s \rightarrow 3d$ transition (inset in Fig. 3b). The intensity of this peak increases for the charged sample and decreases for the discharged sample.

3.2 EXAFS

Fig. 4a shows the k^3 -weighted $\chi(k)$ signals at the Mn K-edge of the material. Their corresponding Fourier transforms are presented in Fig. 4b. As can be seen from Fig. 4a, the amplitude of the $\chi(k)$ signal decreases for the sample charged to 4.8 V. The corresponding changes in the Fourier transform involve a preferential reduction in the amplitude of the 1st peak (Mn–O), besides an overall damping of other higher order peaks. However, for the sample discharged to 2.5 V, the amplitude of the EXAFS signals begins to increase again. Qualitatively, the EXAFS signals at the Co K-edge of the pristine, charged and discharged samples appear similar (Fig. 5). There is a systematic decrease in the amplitude of the signal for the sample charged to 4.8 V and an increase for the sample discharged to 2.5 V.

For comparison, the EXAFS data of Li_2MnO_3 and LiCoO_2 reference compounds are presented in Fig. 6. In the pristine state, the EXAFS data at the Mn K-edge of the material appear similar to those of the Li_2MnO_3 reference compound and, therefore, are explained by the monoclinic structure of Li_2MnO_3 (space group $C2/m$)²¹ as shown in Fig. 7a. Best-fit parameters are reported in Table S1 in the ESI.† The amplitude of the EXAFS signal coming from any coordination shell in the structure primarily depends on the product $S_0^2 \times N$, where N is the number of coordinating atoms in that shell. Therefore, these two parameters for any shell cannot be varied simultaneously in a fit. This can be rationalized from the fact that when the number of oxygen nearest neighbors (O_{n-n}) in a fit to the EXAFS

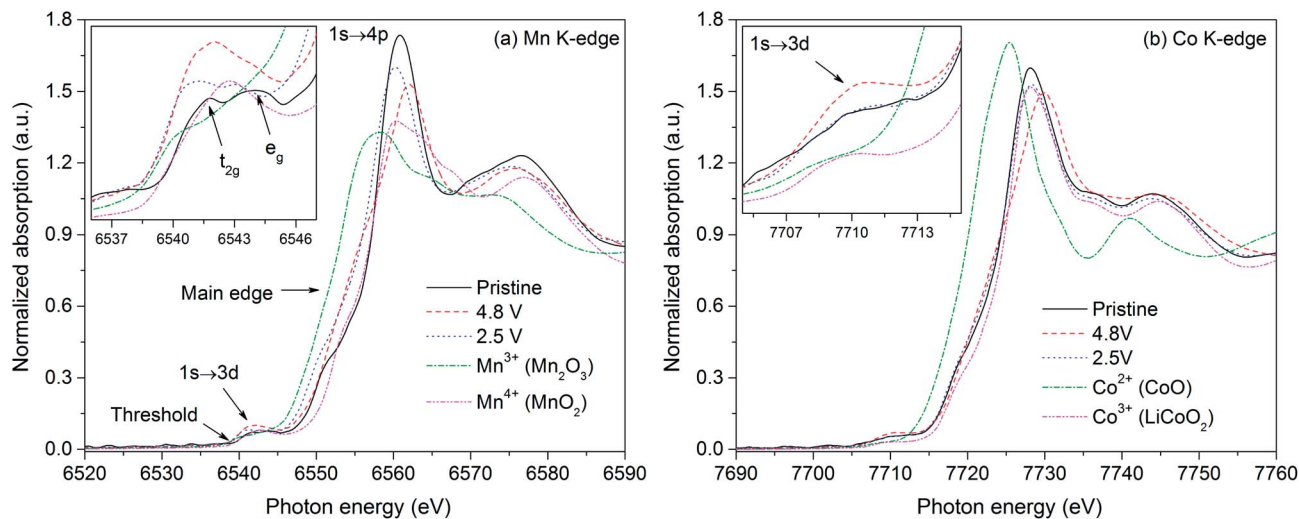


Fig. 3 Normalized absorption spectra at the (a) Mn and (b) Co K-edges of $0.5\text{Li}_2\text{MnO}_3 \cdot 0.5\text{LiCoO}_2$ in the pristine state (solid black line), when charged to 4.8 V (dashed red line) and when discharged to 2.5 V (dotted blue line) along with those of Mn^{3+} , Mn^{4+} , Co^{2+} and Co^{3+} -containing reference compounds. The inset shows an enlarged pre-edge region of these spectra.

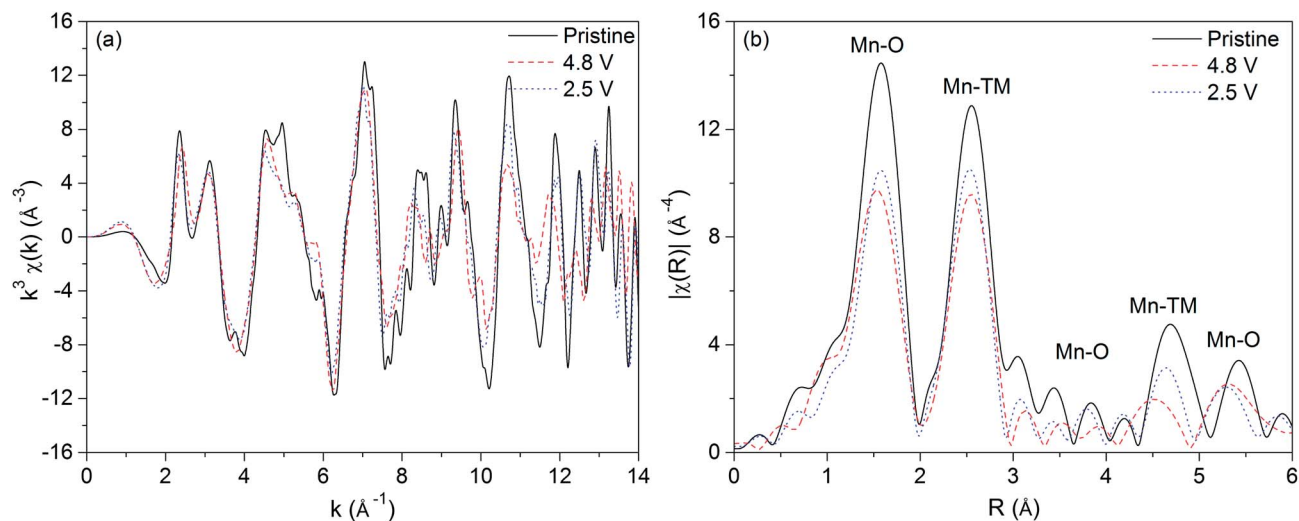


Fig. 4 (a) k^3 -weighted EXAFS signals $\chi(k)$ and (b) their Fourier transforms at the Mn K-edge of $0.5\text{Li}_2\text{MnO}_3 \cdot 0.5\text{LiCoO}_2$ in the pristine state (solid black line), when charged to 4.8 V (dashed red line) and when discharged to 2.5 V (dotted blue line). Discrete data points are presented by lines for the sake of clarity. For raw data, see Fig. 7.

data at the Mn K-edge of the pristine sample was constrained to that obtained from the theoretical model, the fit refined S_0^2 to 0.67(6) which is consistent for Mn absorbers. Conversely, when S_0^2 was constrained to 0.68, the fit refined O_{n-n} to 6.2(7) which is also in agreement with the octahedral coordination of Mn^{4+} ions in Li_2MnO_3 . Moreover, the σ^2 parameter which represents disorder also affects the EXAFS amplitudes. Therefore, the terms $S_0^2 \times N$ and σ^2 for a given shell are highly correlated in a fit. Since S_0^2 is a property of absorbing atoms,^{22–24} it is transferable between compounds with the same absorbing atom–ligand combination, whereas N and σ^2 for any shell can be refined in a fit. Thus, in order to quantify structural changes as a result of any physical or chemical changes that the sample has

undergone, the value of S_0^2 can be constrained to that obtained from the starting material.

The EXAFS data of the sample charged to 4.8 V were explained by a layered MnO_2 structure (space group $R\bar{3}m$) as shown in Fig. 7b. When S_0^2 was constrained to 0.68, the fit refined O_{n-n} to 6.7(6) (Table S2 in the ESI†). The observed increase in the amplitude of the EXAFS signals for the discharged sample suggests structural reordering in the material. Quite consistently, the EXAFS data of the discharged sample were explained by a Li_2MnO_3 structure as shown in Fig. 7c. When S_0^2 was constrained to 0.68, the fit refined O_{n-n} to 4.9(6) (Table S3 in the ESI†). Qualitatively, the EXAFS data at the Co K-edge of the material in the pristine, charged and discharged

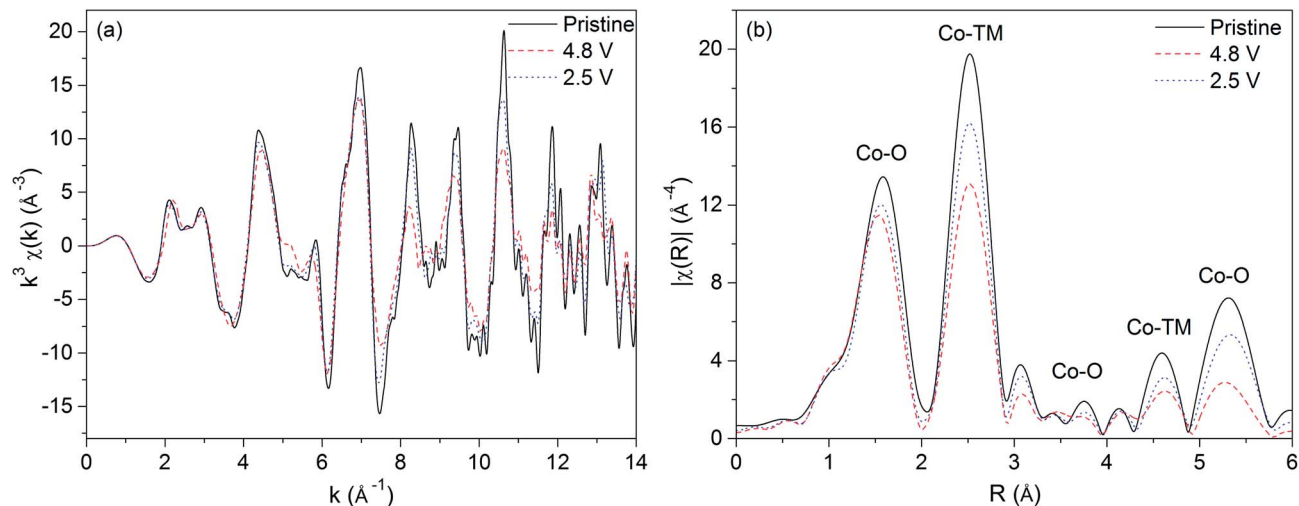


Fig. 5 (a) k^3 -weighted EXAFS signals $\chi(k)$ and (b) their Fourier transforms at the Co K-edge of $0.5\text{Li}_2\text{MnO}_3 \cdot 0.5\text{LiCoO}_2$ in the pristine state (solid black line), when charged to 4.8 V (dashed red line) and when discharged to 2.5 V (dotted blue line). Discrete data points are presented by lines for the sake of clarity. For raw data, see Fig. 8.

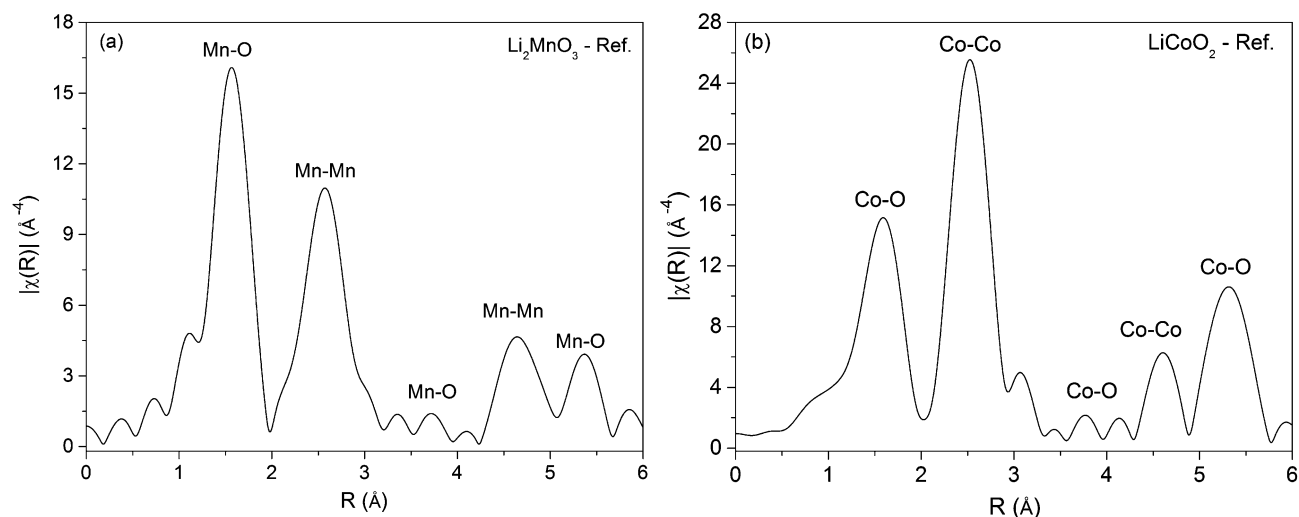


Fig. 6 EXAFS data at the (a) Mn K-edge of Li_2MnO_3 and (b) Co K-edge of LiCoO_2 reference compounds.

states appear similar to those of the LiCoO_2 reference compound. Therefore, a layered structure of LiCoO_2 (ref. 25) could explain the data of all these states (Fig. 8). Best-fit parameters are presented in Tables S4 to S6 in the ESI.†

Fig. 9 shows the variation in the average metal–ligand bond length around Mn and Co atoms of $0.5\text{Li}_2\text{MnO}_3 \cdot 0.5\text{LiCoO}_2$ during charge and discharge. As can be seen from Fig. 9a, the average Mn–O bond length in the pristine state is very close to that of $\text{Mn}^{4+}\text{–O}$. However, the observed changes in this bond length during charge and discharge are superimposed by large uncertainties. Quite contrarily, changes in the average Co–O bond length (Fig. 9b) are large and clearly follow a reversible trend. In the pristine state, the average Co–O bond length is similar to that of $\text{Co}^{3+}\text{–O}$. For the charged sample, this bond length decreases, while for the discharged sample it increases and becomes similar to that of the pristine sample.

Fig. 10 shows the variation in the σ^2 parameter of various coordination shells around Mn and Co atoms of $0.5\text{Li}_2\text{MnO}_3 \cdot 0.5\text{LiCoO}_2$ during charge and discharge. The term σ^2 represents the distribution of the backscattering atoms around their mean position and accounts for both thermal vibrations (thermal disorder) and static displacements (structural disorder) of atoms.^{27,28} Since all samples in the present study are characterized at the same temperature (*i.e.* room temperature), a systematic variation in their σ^2 parameters can be attributed to varying structural disorder of the material as a result of electrochemical cycling, neglecting thermal disorder. As can be seen from Fig. 10a, structural disorder around Mn and Co atoms follows a trend. The pristine sample has the lowest, while the charged sample has the highest disorder. Structural disorder for the discharged sample is intermediate and appears to revert to that of the pristine sample.

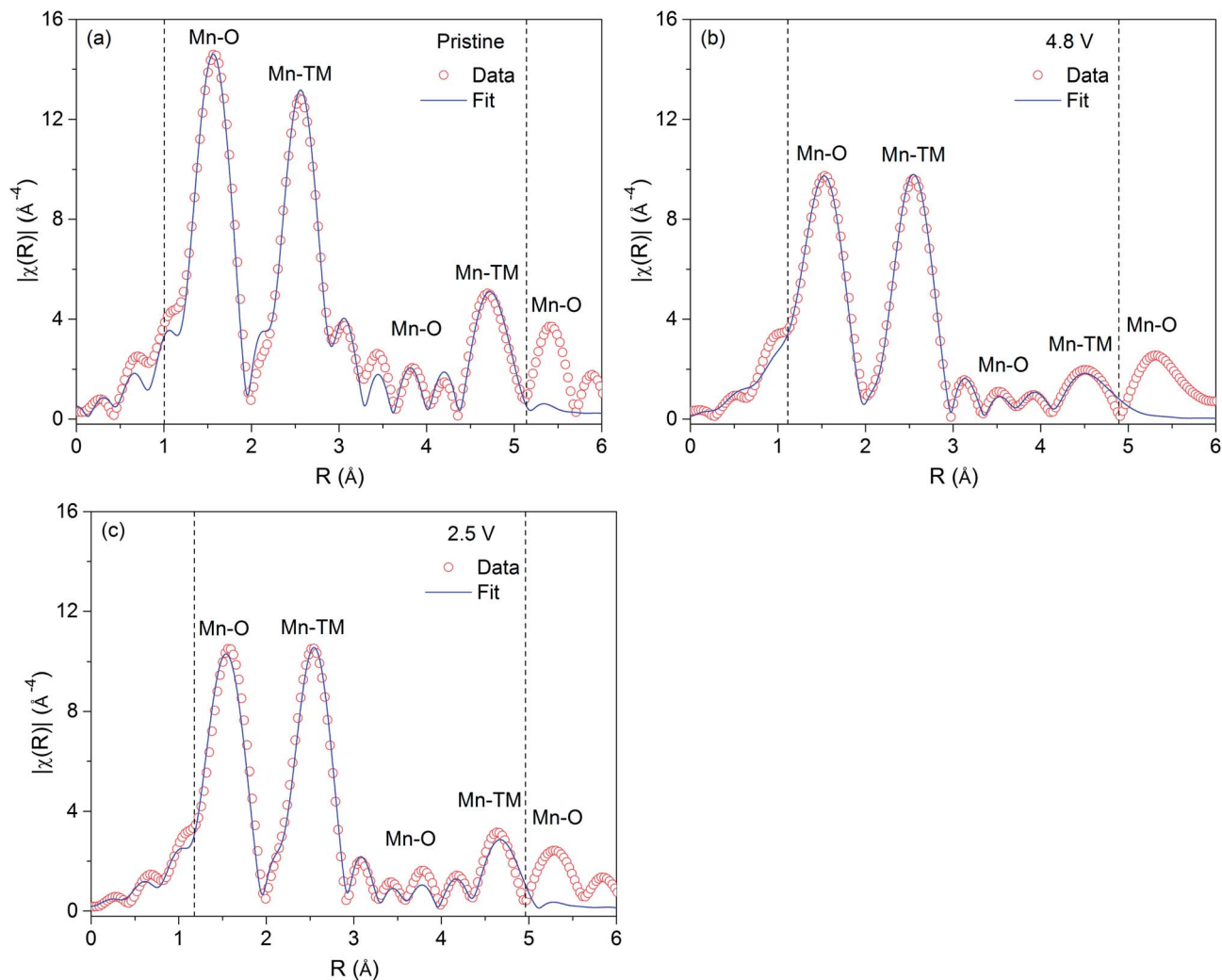


Fig. 7 EXAFS fits to the data measured at the Mn K-edge of 0.5Li₂MnO₃·0.5LiCoO₂ in the (a) pristine state, (b) when charged to 4.8 V and (c) when discharged to 2.5 V. The dotted lines indicate the fitting range.

The statistical EXAFS fit parameters at the Mn and Co K-edges of the material are reported in Table S7 in the ESI.† Good agreement between data and theory for all samples can be seen from their *R*-factors that are ≤ 0.02 .

4 Discussion

4.1 XANES

Empirically, chemical shifts in the absorption spectra are widely used to estimate changes in the valence of absorbing atoms.^{29–35} However, this approach has often proved to be subjective^{33,34} and confusing,³⁵ since in addition to the valence of absorbing atoms, chemical shifts are also affected by other factors such as type, symmetry and number of nearest neighbors, character of bond *etc.*²⁹ Furthermore, the relative contribution of each of these factors to the observed chemical shifts varies widely from one absorbing atom type to another in a material. This can be realized by observing the XANES region at the Mn and Co K-edges of various samples of 0.5Li₂MnO₃·0.5LiCoO₂ in Fig. 3. The observed shift in the position of the 1s → 4p peak at the Mn

K-edge of the charged sample to higher energy, suggesting the oxidation of Mn⁴⁺ ions of the Li₂MnO₃ component, is energetically unfavorable due to the intrinsic electronic configuration of Mn⁴⁺ ions in octahedral coordination.¹⁶ Moreover, the cross-over of spectra along the main edge complicates the interpretation of chemical shifts, since the estimation of the valence state depends on the reference point chosen. On the other hand, chemical shifts among various spectra at the Co K-edge unequivocally suggest the oxidation of Co³⁺ ions of the LiCoO₂ component to Co⁴⁺ during charge and the reduction of Co⁴⁺ ions back to Co³⁺ during discharge. Thus, a fingerprint approach of estimating valence of absorbing atoms based on the observed chemical shifts yields different conclusions at the Mn and Co K-edges and, hence, is ambiguous. In contrast to this, changes in the metal–ligand bond length provide direct evidence of changes in the valence of TM ions,³⁶ since this bond length primarily depends on the average ionic radius of TM ions, which, in turn, depends on their average valence state. Therefore, the observed chemical shifts at the Mn and Co

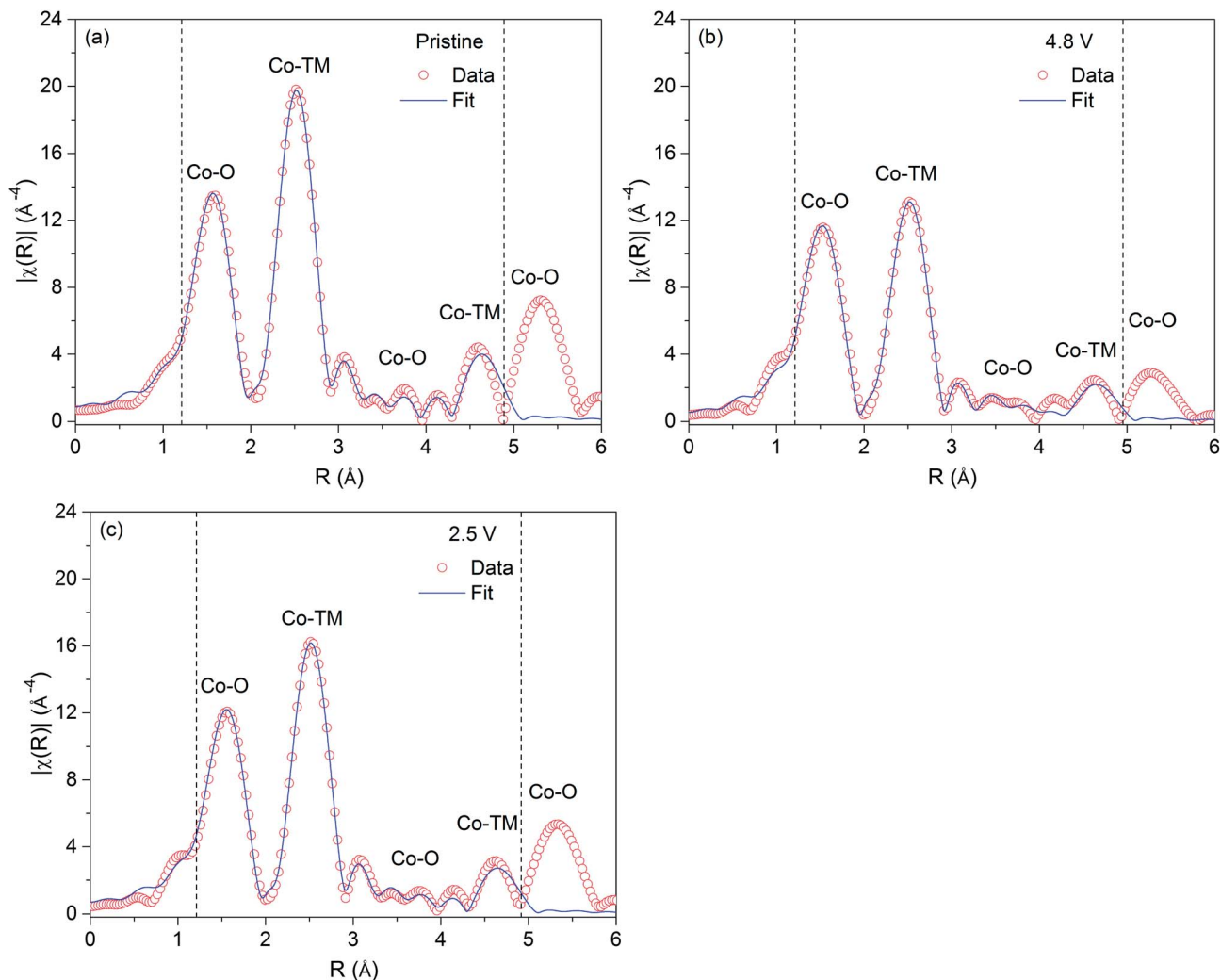


Fig. 8 EXAFS fits to the data measured at the Co K-edge of $0.5\text{Li}_2\text{MnO}_3 \cdot 0.5\text{LiCoO}_2$ in the (a) pristine state, (b) when charged to 4.8 V and (c) when discharged to 2.5 V.

K-edges will be discussed further in conjunction with changes in the average metal–ligand bond length around these TM ions.

4.2 EXAFS

In order to elucidate structural changes in $0.5\text{Li}_2\text{MnO}_3 \cdot 0.5\text{LiCoO}_2$, it is important to first understand atomic arrangements of its individual components. Both Li_2MnO_3 and LiCoO_2 have a layered O3 structure, with the close-packed oxygen layers arranged in an ABCABC sequence and the inter-slab region occupied by Li^+ ions only. However, the major difference between these two structures lies in the atomic arrangement of their slab layers. There is an ordering of Li^+ and Mn^{4+} ions within the slab layers of Li_2MnO_3 , while the slab layers of LiCoO_2 are occupied by Co^{3+} ions only. This difference in the atomic arrangement of the slab layers of these compounds gives rise to different local atomic environments around their TM ions, which can be clearly seen from the distinct EXAFS signals at the Mn and Co K-edges of Li_2MnO_3 and LiCoO_2 reference compounds in Fig. 6.

Qualitatively, the EXAFS data at the Mn (Fig. 7a) and Co (Fig. 8a) K-edges of the pristine sample appear similar to those of Li_2MnO_3 (Fig. 6a) and LiCoO_2 (Fig. 6b) reference compounds, respectively, suggesting that atomic arrangements around Mn and Co atoms of the material are similar to those in Li_2MnO_3 and LiCoO_2 . These results confirm that both Li_2MnO_3 and LiCoO_2 components of the material exist as physically separate domains. However, the ratio of the amplitude of the first two Fourier transform peaks at the Mn K-edge, *i.e.* $\frac{\text{Mn-O}}{\text{Mn-TM}}$, which is the characteristic EXAFS feature of Li_2MnO_3 and represents its ordered atomic arrangements,²⁶ is lower for the pristine sample than for the Li_2MnO_3 reference compound. This reduction in the $\frac{\text{Mn-O}}{\text{Mn-TM}}$ ratio stems from a decrease in the amplitude of the 1st peak of Mn–O and an increase in the amplitude of the 2nd peak of Mn–TM relative to those of the Li_2MnO_3 reference compound. The decreased amplitude of the 1st peak corresponds to increased disorder in the arrangement of oxygen atoms of Li_2MnO_3 domains, while the increased amplitude of the 2nd peak suggests the presence of an element

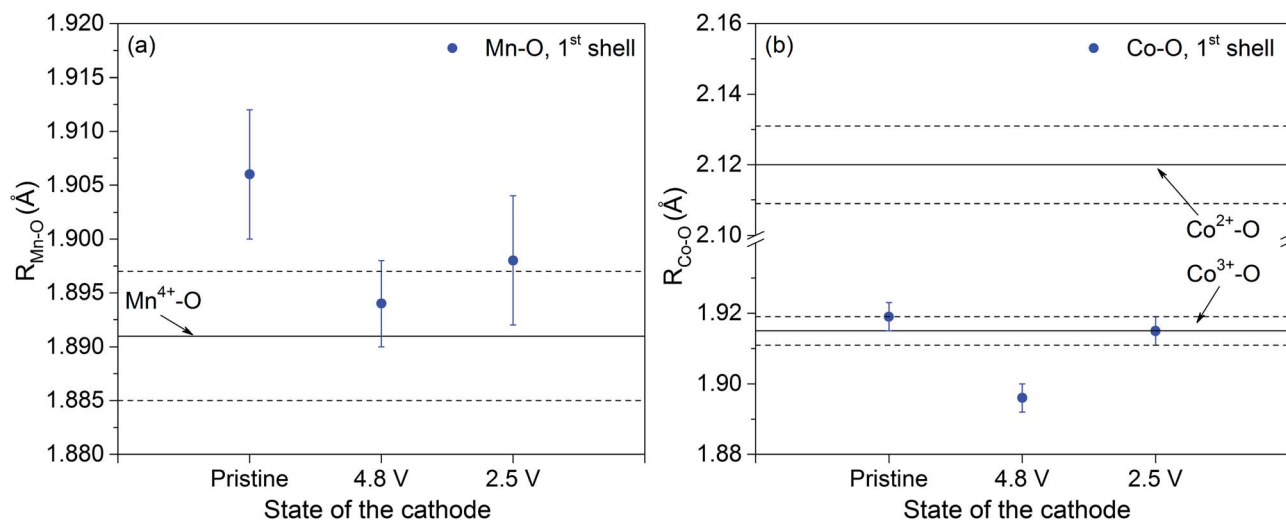


Fig. 9 Average metal–ligand bond length around (a) Mn and (b) Co atoms of $0.5\text{Li}_2\text{MnO}_3 \cdot 0.5\text{LiCoO}_2$ in the pristine, charged and discharged states. The solid line in (a) indicates the average $\text{Mn}^{4+}\text{-O}$ (metal–ligand) bond length obtained from the literature,²⁶ while those in (b) indicate the average $\text{Co}^{2+}\text{-O}$ and $\text{Co}^{3+}\text{-O}$ bond lengths obtained by fitting the EXAFS data of CoO and LiCoO_2 reference compounds (refer to Fig. S1 and Table S8 in the ESI†). The dotted lines represent uncertainties in the fitted value.

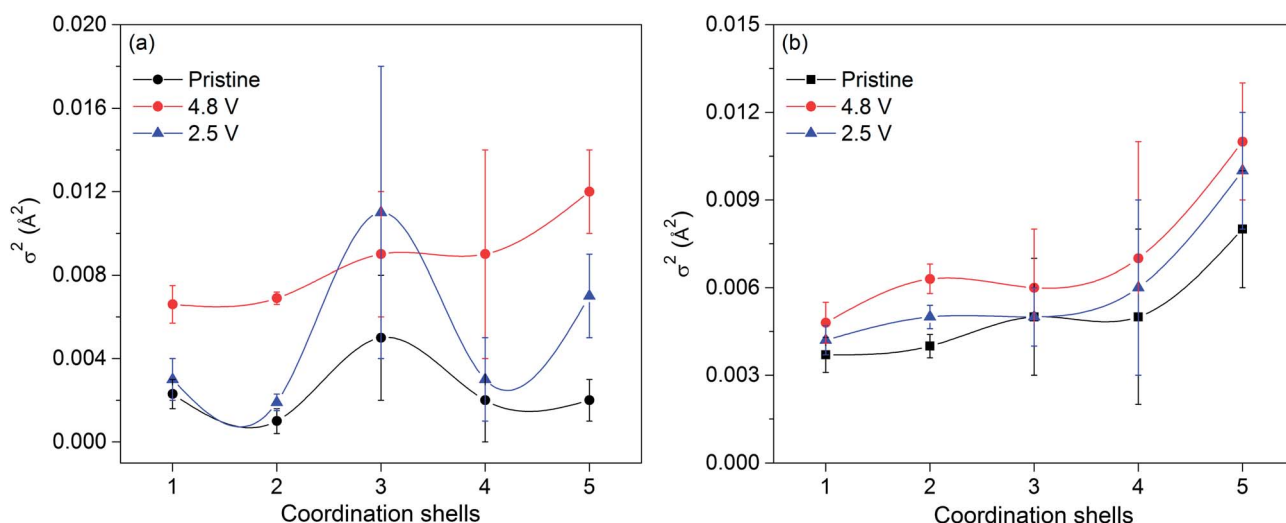


Fig. 10 Structural disorder around (a) Mn and (b) Co atoms of $0.5\text{Li}_2\text{MnO}_3 \cdot 0.5\text{LiCoO}_2$ in the pristine, charged and discharged states. Lines are guide to eyes.

with a higher atomic number (Z) such as Co along with Mn in the 2nd shell due to some substitution of Mn by Co in the slab layers of Li_2MnO_3 domains. As shown in Fig. 1, with increasing Co content, all XRD peaks of lithium-rich materials shift to higher angle towards those of LiCoO_2 and the superlattice reflections originating from Li_2MnO_3 domains gradually disappear. These results suggest that higher Co contents tend to reduce the amount of Li_2MnO_3 -type domains in lithium-rich materials, giving rise to the formation of a $\text{Li}_{(1+x)}\text{MO}_2$ -type structure. However, the presence of superlattice reflections in the XRD pattern of $0.5\text{Li}_2\text{MnO}_3 \cdot 0.5\text{LiCoO}_2$ despite its higher Co content and similarities in atomic arrangements around its Mn atoms to those in Li_2MnO_3 confirm that both Li_2MnO_3 and LiCoO_2 components of the material exist as separate domains.

However, there may be some exchange between Mn and Co atoms in the slab layers of these domains as shown in Fig. 11.

As can be seen from Fig. 2, a specific capacity of 308 mA h g^{-1} delivered by the cell during activation of $0.5\text{Li}_2\text{MnO}_3 \cdot 0.5\text{LiCoO}_2$ is significantly high, considering the true electrochemical contribution of both Li_2MnO_3 and LiCoO_2 components to it. The Li_2MnO_3 component of the material is considered electrochemically inactive,³⁷ since lithium extraction in a conventional way by oxidizing octahedrally coordinated Mn^{4+} ions is energetically unfavored.¹⁶ Furthermore, even complete lithium deintercalation of the 0.5LiCoO_2 component would not result in a specific capacity more than 140 mA h g^{-1} . Thus, there is a need to understand the origin of high capacities delivered by lithium-rich cathode materials. The observed changes in the

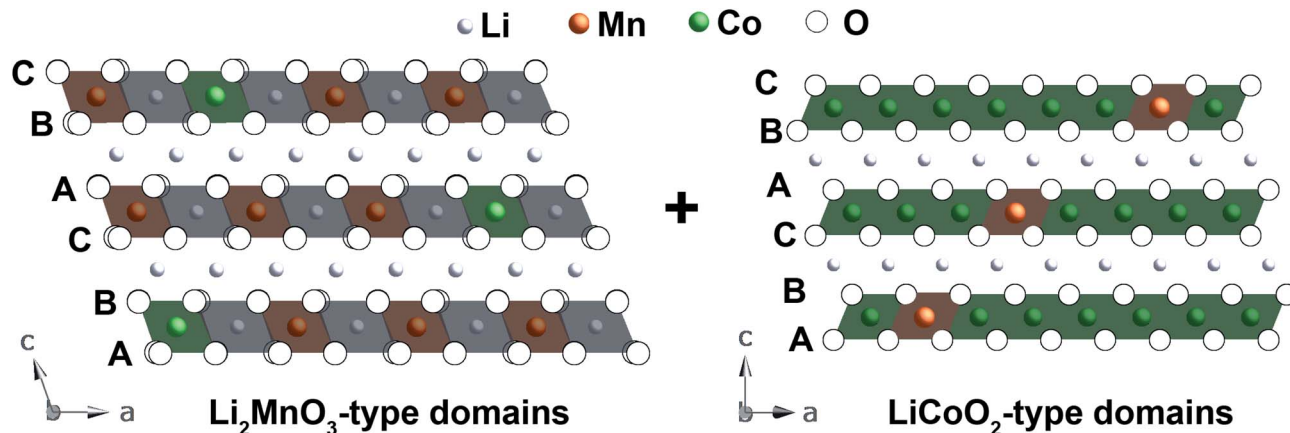


Fig. 11 Proposed atomic arrangements in Li_2MnO_3 and LiCoO_2 domains of $0.5\text{Li}_2\text{MnO}_3 \cdot 0.5\text{LiCoO}_2$.

EXAFS signals at the Mn K-edge of the material during charge and discharge (Fig. 4) clearly suggest structural modifications occurring in Li_2MnO_3 domains during lithium extraction and/or reinsertion. A preferential reduction in the amplitude of the 1st peak corresponding to oxygen atoms in the 1st shell around Mn absorbers, besides an overall damping of other higher order peaks for the charged sample (Fig. 4b), is consistent with those observed during an independent XAS investigation of Li_2MnO_3 .²⁶ These changes have been attributed to a simultaneous removal of oxygen along with lithium during activation of Li_2MnO_3 , giving rise to the formation of a disordered MnO_2 -type structure.²⁶ The best fit to the EXAFS data of the charged sample by a layered MnO_2 structure (Fig. 7b) and an increase in the σ^2 parameter of various coordination shells around Mn absorbers (Fig. 10a) confirm the similar structural changes as a result of a combined loss of lithium and oxygen (as “ Li_2O ”) from Li_2MnO_3 domains of the material during activation. However, despite the oxygen release, the fit for the charged sample refined O_{n-n} to an unreasonably high value of 6.7(6). This can be attributed to a high correlation of the order of 0.89 between the σ^2 and O_{n-n} of the 1st shell. Since atomic rearrangements caused by oxygen release increase the σ^2 parameter of the 1st shell (Fig. 10a), the fit systematically overestimates the value of O_{n-n} for the charged sample. A similar difficulty in determining the number of nearest neighbors for disordered states of a system has been reported previously.³⁸ A subtle reduction in the average Mn–O bond length of the charged sample can be attributed to changing atomic arrangements around Mn absorbers due to oxygen release. This is also consistent with the observed change in the shape and intensity of the pre-edge peaks of the charged sample (see the inset in Fig. 3a), since the pre-edge region is extremely sensitive to changes in the local coordination symmetry around absorbing atoms.^{26,29} However, the amount of O_2 -gas released during activation of lithium-rich materials is found to be much lesser than expected, when accounting only oxygen release to the entire charge capacity.^{12,13} These results suggest contributions from other unusual processes such as partial oxidation of oxygen anions^{35,39–41} and electrolyte oxidation.^{42–44} Protons generated as a result of electrolyte oxidation

may displace Li^+ ions from Li_2MnO_3 domains.^{45–49} A similar $\text{Li}^+ - \text{H}^+$ exchange mechanism has been reported for LiMn_2O_4 (ref. 50 and 51) and lithium-rich cathode material.⁵² However, the clear driving force behind such an ion-exchange process remains unknown. It is important to mention that EXAFS cannot directly confirm the presence of either H^+ or Li^+ ions in the material due to very low backscattering power of these light elements, but local distortions caused by the presence of protons in delithiated samples of Li_2MnO_3 ^{45–49} have been readily detected by EXAFS.²⁶

The observed increase in the amplitude of the EXAFS signals at the Mn K-edge for the discharged sample (Fig. 4) suggests structural reordering around Mn atoms of the material during lithium reinsertion. This is consistent with a decrease in the σ^2 parameter of various coordination shells around Mn absorbers (Fig. 10a). However, since permanent disorder induced in the material by an irreversible oxygen release cannot be reverted, the discharged sample exhibits slightly higher disorder and, as a result, a slightly damped amplitude of its EXAFS signals compared to the pristine sample (Fig. 4). The best-fit to the EXAFS data of the discharged sample is by a Li_2MnO_3 structure and refines O_{n-n} to 4.9(6). These results suggest that atomic rearrangements caused by lithium reinsertion into the layered MnO_2 -type structure gives rise to the formation of a Li_2MnO_3 -type structure which is oxygen-deficient. These results are in agreement with the observed similarities in the pre-edge region of the pristine and discharged samples (inset in Fig. 3a), confirming that the structure regains its original ordered configuration during lithium reinsertion. Correspondingly, the σ^2 parameter of the 1st shell decreases and, therefore, unlike the charged sample, the fit for the discharged sample could correctly estimate oxygen deficiency in the material. However, the σ^2 parameter of the 3rd shell remains significantly high and ill-refined upon discharge. This may be attributed to a permanent distortion in the arrangement of oxygen layers caused by the ion-exchange process. The average Mn–O bond length upon discharge effectively remains unchanged from that of the charged sample, which rules out the proposed reduction of Mn^{4+} to Mn^{3+} during lithium reinsertion into the layered

MnO₂-type structure.^{6,48} This result is in agreement with the previous report of Robertson and Bruce⁴⁶ that the average valence state of Mn in Li₂MnO₃ remains unchanged at 4+ during charge and discharge. A specific capacity of 252 mA h g⁻¹ delivered by the cell during discharge clearly suggests that a significant amount of lithium is reinserted into the layered MnO₂-type structure. However, in the absence of a conventional redox reaction, the reinserted lithium could have been charge-compensated by the reduction of partially oxidized oxygen anions of the active material^{26,35,40,41} together with that of electrolyte solvent species at the cathode–electrolyte interface which may consume protons driven out of the structure during lithium reinsertion.⁴⁶ In fact, the structural reordering observed around Mn atoms of the material during discharge is consistent with that observed for Li₂MnO₃ (ref. 26, 53 and 54) and has been specifically attributed to the relaxation of strained oxygen layers caused by the ion-exchange process during discharge.²⁶ The observed loss of capacity in the 1st cycle can be attributed to a permanent removal of oxygen along with lithium from Li₂MnO₃ domains of the material during activation and should not be confused with an irreversible consumption of lithium in the formation of the solid electrolyte interface (SEI), since there is an infinite supply of lithium ions in the form of lithium-metal anode in a half-cell configuration.

Complete lithium deintercalation from LiCoO₂ gives rise to the transition of its original O3 structure to an O1 structure where the stacking sequence of close-packed oxygen layers is altered from an ABCABC to ABABAB.⁵⁵ A similar observation has been reported for other isostructural LiMO₂ (M = TM ions) cathode materials.^{56–58} It has been reported that a transition from the O3 to O1 structure proceeds with a gradual slippage between the MO₂ slabs, forming O1-type stacking faults. As the degree of lithium deintercalation increases, the extent of O1-type stacking faults within the O3 structure also increases until the entire O3 structure is converted to an O1-type structure.^{56,57} The observed reduction in the amplitude of the Fourier transform peaks at the Co K-edge of the charged sample suggests increased structural disorder in the deintercalated Li_xCoO₂ domains as a result of the formation of O1-type stacking faults. Quite consistently, the σ^2 parameter for various coordination shells around Co atoms increases (Fig. 10b). However, the fact that the charged sample retains the same characteristic EXAFS features as the pristine sample despite a reduction in the amplitude suggests only partial lithium deintercalation from LiCoO₂ domains and thereby, an incomplete transition of their O3 structure to O1-type structure even at a potential as high as 4.8 V. Previously, similar layered LiMn_{1/3}Ni_{1/3}Co_{1/3}O₂ (ref. 58) and LiMn_{0.4}Ni_{0.4}Co_{0.2}O₂ (ref. 59) cathode materials were observed to undergo an irreversible transition of their O3 structure to O1, when subjected to excessive lithium deintercalation by charging to 4.8 V. These results highlight the role of the Li₂MnO₃ component in lithium-rich cathode materials. In the case of 0.5Li₂MnO₃·0.5LiCoO₂, the total electrochemical “load” is divided between the two components: Li₂MnO₃ and LiCoO₂. Clearly, lithium extraction from Li₂MnO₃ domains, though *via* unusual electrochemical processes, enables LiCoO₂ domains to sustain a higher cut-off voltage

without undergoing excessive lithium deintercalation and thereby, irreversible structural changes. The observed increase in the intensity of the pre-edge peak at the Co K-edge of the charged sample (Fig. 3b) suggests a reduction in the metal–ligand bond length around Co atoms of the material.^{26,29,36} This is further complemented by an unambiguous reduction in the average Co–O bond length (Fig. 9b) and a clear shift in the position of the 1s → 4p peak to higher energy at the Co K-edge of the charged sample. All these results confirm oxidation of Co³⁺ ions to Co⁴⁺ during lithium deintercalation from LiCoO₂ domains.

Lithium intercalation into an O1 structure is energetically unfavorable, since in this configuration LiO₆ octahedra share faces with the adjoining MO₆ octahedra.⁵⁵ A large electrostatic repulsion between Li⁺ and highly oxidized TM ions makes such a configuration unstable. In contrast to this, lithium intercalation into an O3 structure gives rise to edge-sharing LiO₆ and MO₆ octahedra with minimum electrostatic repulsion and thereby, improved stability. Thus, lithium intercalation reverts O1-type stacking faults back to the original O3-type.^{56,57} This is confirmed by the observed increase in the amplitude of the EXAFS signals of the discharged sample, suggesting a reduction in structural disorder. Correspondingly, the σ^2 parameter for various coordination shells around Co atoms of the discharged sample decreases. These results confirm the conversion of O1-type stacking faults back to the original O3-type during lithium intercalation into Li_xCoO₂ domains. However, the amplitude of the EXAFS signal corresponding to the discharged sample remains slightly damped compared to that of the pristine sample, indicating that a complete conversion from O1 to O3-type structure has not occurred and the resultant structure at 2.5 V may contain some O1-type stacking faults. An increasing average Co–O bond length for the discharged sample is consistent with the reduced intensity of the pre-edge peak and a reverse shift in the position of the 1s → 4p peak at the Co K-edge (Fig. 3b). All these results confirm reduction of Co⁴⁺ ions to Co³⁺ during lithium intercalation into Li_xCoO₂ domains.

5 Conclusions

XAS investigation of electrochemically cycled samples of 0.5Li₂MnO₃·0.5LiCoO₂ provides a deeper insight into the structural and electrochemical aspects of this cathode material. Local atomic arrangements around Mn and Co atoms of the material clearly suggest that both Li₂MnO₃ and LiCoO₂ components exist as separate domains. However, there may be some exchange of TM ions in the slab layers of these domains. Lithium extraction from Li₂MnO₃ domains occurs with a concurrent removal of oxygen, giving rise to the formation of a layered MnO₂-type structure. A large irreversible capacity obtained during activation of the material can be attributed to this combined loss of lithium and oxygen from Li₂MnO₃ domains. Moreover, partial oxidation of oxygen anions and/or electrolyte oxidation may also contribute to the observed charge capacity during activation of the material. Atomic rearrangements caused by lithium reinsertion into the layered MnO₂-type structure gives rise to the formation of a Li₂MnO₃-type structure

which is lithium and oxygen deficient. The average valence state of manganese ions remains unchanged at 4+ during charge and discharge. On the other hand, lithium deintercalation from LiCoO₂ domains gives rise to the formation of O1-type stacking faults within their O3 structure with the concomitant oxidation of Co³⁺ ions to Co⁴⁺. Lithium intercalation into Li_xCoO₂ domains reverts O1-type stacking faults back to the original O3-type and reduction of Co⁴⁺ ions to Co³⁺ occurs. The randomly distributed Li₂MnO₃ domains act as sources of excess lithium, enabling LiCoO₂ domains to sustain an upper cut-off voltage as high as 4.8 V without experiencing irreversible structural changes.

Acknowledgements

J.R., G.S. and J.B. gratefully acknowledge financial support from the Europäischer Fonds für regionale Entwicklung (EFRE) under the project BATMAT (no. 200720132/35). R.K. and J.L. acknowledge financial support from the Hans-L. Merkle Stiftung of the Robert Bosch GmbH and the project KaLiPat. The authors thank Dr Ivo Zizak and Dr Maria Brzhezinskaya for their assistance during beamtime.

References

- C. Johnson, J.-S. Kim, C. Lefief, N. Li, J. Vaughey and M. Thackeray, *Electrochem. Commun.*, 2004, **6**, 1085–1091.
- C. Johnson, N. Li, J. Vaughey, S. Hackney and M. Thackeray, *Electrochem. Commun.*, 2005, **7**, 528–536.
- M. Thackeray, S.-H. Kang, C. Johnson, J. Vaughey and S. Hackney, *Electrochem. Commun.*, 2006, **8**, 1531–1538.
- C. Johnson, *J. Power Sources*, 2007, **165**, 559–565.
- C. Johnson, N. Li, C. Lefief and M. Thackeray, *Electrochem. Commun.*, 2007, **9**, 787–795.
- M. Thackeray, S.-H. Kang, C. Johnson, J. Vaughey, R. Benedek and S. Hackney, *J. Mater. Chem.*, 2007, **17**, 3112–3125.
- J. Li, R. Klöpsch, M. Stan, S. Nowak, M. Kunze, M. Winter and S. Passerini, *J. Power Sources*, 2011, **196**, 4821–4825.
- J. Croy, M. Balasubramanian, D. Kim, S.-H. Kang and M. Thackeray, *Chem. Mater.*, 2011, **23**, 5415–5424.
- J. Bareño, M. Balasubramanian, S. Kang, J. Wen, C. Lei, S. Pol, I. Petrov and D. Abraham, *Chem. Mater.*, 2011, **23**, 2039–2050.
- J. Croy, D. Kim, M. Balasubramanian, K. Gallagher, S.-H. Kang and M. Thackeray, *J. Electrochem. Soc.*, 2012, **159**, A781–A790.
- K. Jarvis, Z. Deng, L. Allard, A. Manthiram and P. Ferreira, *Chem. Mater.*, 2011, **23**, 3614–3621.
- A. Armstrong, M. Holzapfel, P. Novák, C. Johnson, S.-H. Kang, M. Thackeray and P. Bruce, *J. Am. Chem. Soc.*, 2006, **128**, 8694–8698.
- N. Yabuuchi, K. Yoshii, S.-T. Myung, I. Nakai and S. Komaba, *J. Am. Chem. Soc.*, 2011, **133**, 4404–4419.
- Y.-S. Hong, Y. Park, K. Ryu, S. Chang and M. Kim, *J. Mater. Chem.*, 2004, **14**, 1424–1429.
- T. Ohzuku, M. Nagayama, K. Tsuji and K. Ariyoshi, *J. Mater. Chem.*, 2011, **21**, 10179–10188.
- J. Saint, M. Doeff and J. Reed, *J. Power Sources*, 2007, **172**, 189–197.
- S. Kelly, D. Hesterberg and B. Ravel, *Methods of Soil Analysis, Part 5 – Mineralogical Methods*, Soil Science Society of America, Madison, WI, USA, 2008, vol. 5, pp. 387–463.
- B. Ravel and M. Newville, *J. Synchrotron Radiat.*, 2005, **12**, 537–541.
- A. Ankudinov, B. Ravel, J. Rehr and S. Conradson, *Phys. Rev. B: Condens. Matter Mater. Phys.*, 1998, **58**, 7565–7576.
- S. Calvin, PhD thesis, The City University of New York, 2001.
- P. Strobel and B. Lambert-Andron, *J. Solid State Chem.*, 1988, **75**, 90–98.
- J. Rehr, E. Stern, R. Martin and E. Davidson, *Phys. Rev. B: Solid State*, 1978, **17**, 560–565.
- E. Stern, B. Bunker and S. Heald, *Phys. Rev. B: Condens. Matter Mater. Phys.*, 1980, **21**, 5521–5539.
- B. Teo, *EXAFS: Basic Principles and Data Analysis*, Springer-Verlag Berlin, 1986, vol. 10.
- J. Akimoto, Y. Gotoh and Y. Oosawa, *J. Solid State Chem.*, 1998, **141**, 298–302.
- J. Rana, M. Stan, R. Kloepsch, J. Li, G. Schumacher, E. Welter, I. Zizak, J. Banhart and M. Winter, *Adv. Energy Mater.*, 2013, DOI: 10.1002/aenm.201300998, in press.
- D. Sayers, E. Stern and F. Lytle, *Phys. Rev. Lett.*, 1971, **27**, 1204–1207.
- J. Rehr and R. Albers, *Rev. Mod. Phys.*, 2000, **72**, 621–654.
- J. Wong, F. Lytle, R. Messmer and D. Maylotte, *Phys. Rev. B: Condens. Matter Mater. Phys.*, 1984, **30**, 5596–5610.
- V. Sapre and C. Mande, *J. Phys. C: Solid State Phys.*, 1972, **5**, 793–797.
- C. Johnson and A. Kropf, *Electrochim. Acta*, 2002, **47**, 3187–3194.
- A. Deb, U. Bergmann, E. Cairns and S. Cramer, *J. Synchrotron Radiat.*, 2004, **11**, 497–504.
- D. Yu, K. Yanagida, Y. Kato and H. Nakamura, *J. Electrochem. Soc.*, 2009, **156**, A417–A424.
- D. Yu and K. Yanagida, *J. Electrochem. Soc.*, 2011, **158**, A1015–A1022.
- A. Ito, Y. Sato, T. Sanada, M. Hatano, H. Horie and Y. Ohsawa, *J. Power Sources*, 2011, **196**, 6828–6834.
- J. Rana, S. Glatthaar, H. Gesswein, N. Sharma, J. Binder, R. Chernikov, G. Schumacher and J. Banhart, *J. Power Sources*, 2014, **255**, 439–449.
- M. Thackeray, *Prog. Solid State Chem.*, 1997, **25**, 1–71.
- B. Ravel and S. Kelly, *AIP Conf. Proc.*, 2007, **882**, 150–152.
- J. Goodenough and Y. Kim, *Chem. Mater.*, 2010, **22**, 587–603.
- H. Koga, L. Croguennec, M. Ménétrier, P. Mannessiez, F. Weill and C. Delmas, *J. Power Sources*, 2013, **236**, 250–258.
- H. Koga, L. Croguennec, M. Ménétrier, K. Douhil, S. Belin, L. Bourgeois, E. Suard, F. Weill and C. Delmas, *J. Electrochem. Soc.*, 2013, **160**, A786–A792.
- K. Kanamura, S. Toriyama, S. Shiraishi and Z.-i. Takehara, *J. Electrochem. Soc.*, 1996, **143**, 2548–2558.
- K. Kanamura, *J. Power Sources*, 1999, **81–82**, 123–129.

- 44 M. Moshkovich, M. Cojocaru, H. Gottlieb and D. Aurbach, *J. Electroanal. Chem.*, 2001, **497**, 84–96.
- 45 A. Robertson and P. Bruce, *Chem. Commun.*, 2002, 2790–2791.
- 46 A. Robertson and P. Bruce, *Chem. Mater.*, 2003, **15**, 1984–1992.
- 47 A. Armstrong, A. Robertson and P. Bruce, *J. Power Sources*, 2005, **146**, 275–280.
- 48 Y. Paik, C. Grey, C. Johnson, J.-S. Kim and M. Thackeray, *Chem. Mater.*, 2002, **14**, 5109–5115.
- 49 W. Tang, H. Kanoh, X. Yang and K. Ooi, *Chem. Mater.*, 2000, **12**, 3271–3279.
- 50 Q. Feng, Y. Miyai, H. Kanoh and K. Ooi, *Langmuir*, 1992, **8**, 1861–1867.
- 51 B. Ammundsen, P. Aitchison, G. Burns, D. Jones and J. Rozière, *Solid State Ionics*, 1997, **97**, 269–276.
- 52 S.-H. Kang, C. Johnson, J. Vaughey, K. Amine and M. Thackeray, *J. Electrochem. Soc.*, 2006, **153**, A1186–A1192.
- 53 M. Rossouw, D. Liles and M. Thackeray, *J. Solid State Chem.*, 1993, **104**, 464–466.
- 54 R. Wang, X. He, L. He, F. Wang, R. Xiao, L. Gu, H. Li and L. Chen, *Adv. Energy Mater.*, 2013, 1–10.
- 55 G. Amatucci, *J. Electrochem. Soc.*, 1996, **143**, 1114.
- 56 L. Croguennec, C. Poullerie and C. Delmas, *J. Electrochem. Soc.*, 2000, **147**, 1314–1321.
- 57 L. Croguennec, C. Poullerie, A. N. Mansour and C. Delmas, *J. Mater. Chem.*, 2001, **11**, 131–141.
- 58 S.-C. Yin, Y.-H. Rho, I. Swainson and L. Nazar, *Chem. Mater.*, 2006, **18**, 1901–1910.
- 59 J. Rana, PhD thesis, Technische Universität Berlin, 2013.